Magnetic Resonance–Based Attenuation Correction for PET/MR Hybrid Imaging Using Continuous Valued Attenuation Maps

Bharath K. Navalpakkam, MSc,† Harald Braun, MSc,† Torsten Kuwert, MD,‡ and Harald H. Quick, PhD†*

Objectives: Attenuation correction of positron emission tomographic (PET) data is critical in providing accurate and quantitative PET volumes. Deriving an attenuation map (μ-map) from magnetic resonance (MR) volumes is a challenge in PET/MR hybrid imaging. The difficulty lies in differentiating cortical bone from air from standard MR sequences because both these classes yield little to no MR signal and thus shows no distinguishable information. The objective of this contribution is 2-fold: (1) to generate and evaluate a continuous valued computed tomography (CT)–like attenuation map (μ-map) with continuous density values from dedicated MR sequences and (2) to compare its PET quantification accuracy with respect to a CT-based attenuation map as the criterion standard and other segmentation-based attenuation maps for studies of the head.

Materials and Methods: Three-dimensional Dixon-volume interpolated breath-hold examination and ultrashort echo time sequences were acquired for each patient on a Siemens 3-T Biograph mMR PET/MR hybrid system and the corresponding patient CT on a Siemens Biograph 64. A pseudo-CT training was done using the epsilon-insensitive support vector regression (ε-SVR) technique on 5 patients who had CT/MR/PET triplets, and the generated model was evaluated on 5 additional patients who were not included in the training process. Four μ-maps were compared, and 3 of them derived from CT: scaled CT ($\mu\text{-map}_{CT}$), 3-class segmented CT without cortical bone ($\mu\text{-map}_{nobone}$), 4-class segmented CT with cortical bone ($\mu\text{-map}_{bone}$), and 1 from MR sequences via ε-SVR technique previously mentioned (ie, MR predicted [$\mu\text{-map}_{MR}$]). Positron emission tomographic volumes with each of the previously mentioned μ-maps were reconstructed, and relative difference images were calculated with respect to $\mu\text{-map}_{CT}$ as the criterion standard.

Results: For PET quantification, the proposed method yields a mean (SD) absolute error of 2.40% (3.69%) and 2.16% (1.77%) for the complete brain and the regions close to the cortical bone, respectively. In contrast, PET using $\mu\text{-map}_{nobone}$ yielded 10.15% (3.31%) and 11.03 (2.26%) for the same, although PET using $\mu\text{-map}_{bone}$ resulted in errors of 3.96% (3.71%) and 4.22% (3.91%). Furthermore, it is shown that the model can be extended to predict pseudo-CTs for other anatomical regions on the basis of only MR information.

Conclusions: In this study, the generation of continuous valued attenuation maps from MR sequences is demonstrated and its effect on PET quantification is evaluated in comparison with segmentation-based μ-maps. A less-than-2-minute acquisition time makes the proposed approach promising for a clinical application for studies of the head. However, further experiments are required to validate and evaluate this technique for attenuation correction in other regions of the body.

Key Words: PET/MR hybrid imaging, attenuation correction, support vector regression, PET quantification

(*Invest Radiol* 2013;48: 323–332)

The advent of hybrid positron emission tomography (PET)/magnetic resonance (MR) systems has opened up the possibility to combine 2 powerful imaging modalities in 1 hybrid imaging device.[1,2] Magnetic resonance imaging (MRI), on the one hand, is known for its excellent soft tissue contrast by means of a plethora of imaging sequences and has the potential to provide highly specific anatomical localization. Positron emission tomography, on the other hand, enables highly specific metabolic imaging. In comparison with PET/computed tomography (CT), PET/MR offers a reduction of radiation dose. Therefore, the hybrid PET/MR system can be a highly beneficial tool for brain and whole-body studies.[3–5] However, MR-based attenuation correction (MRAC) of PET images still remains a problem at large. In PET/CT hybrid imaging, a simple energy scaling from CT energies (40–140 keV) to PET energy (511 keV) is sufficient to generate attenuation maps.[6,7] However, such a relationship is not straightforward in PET/MR imaging because MR measures aspects of protons, whereas PET attenuation is affected by electron density. The main problem in MR-derived attenuation maps is distinguishing between bone and air because these 2 materials offer little to no signal in most MR sequences. However, their linear attenuation coefficients (LACs) vary significantly (air, 0 cm^{-1} and bone, 0.1510 cm^{-1} at 511 keV).

Several different ways of handling this issue have been proposed: Martinez-Möller et al[8] argued that representing the cortical bone as soft tissue does not undermine the clinical value of the attenuation-corrected PET images. According to this study, ignoring the cortical bone resulted in an 8% decrease in standardized uptake value for bone lesions and 4% decrease for head and neck lesions. Schulz et al[9] reported 3-class segmentations (air, tissue, and lung) for whole-body imaging studies, but they did not investigate their μ-map for brain studies. This has raised the question in the research community whether it is necessary or beneficial to consider the cortical bone as an additional class.

In current PET/MR hybrid systems, an attenuation map based on a 3-dimensional (3D) Dixon-VIBE (volume interpolated breath-hold examination) sequence is commonly used. Depending upon the vendor, the μ-map in these systems mainly distinguish between 2 (air, soft tissue) to 3 classes (air, water, and fat) for the head regions.[10,11] For the torso region, lung is identified as an additional class. Because of a relatively fast acquisition, an easily integrable workflow, and a simple segmentation-based approach, this has found wide usage among the first clinical studies of this relatively new hybrid imaging modality. Although the 3D Dixon-VIBE–based μ-map is generally accepted/used for studies of the torso, cortical bone omission for studies of the head has shown to have a significant impact on PET-attenuation correction (AC).[12,13]

Whereas most of the recent research focuses on the effect on PET-AC when including or disregarding a class,[12,14,15] very few MR-based AC implementations, which include bone, have sufficiently

Received for publication August 1, 2012; and accepted for publication, after revision, December 13, 2012.

From the *Pattern Recognition Lab; †Institute of Medical Physics; and ‡Clinic of Nuclear Medicine, Friedrich-Alexander-University Erlangen-Nürnberg, Erlangen, Germany.

Conflicts of interest and sources of funding: Supported by a grant from a research agreement between Siemens Healthcare Sector Erlangen, Germany, and the Friedrich-Alexander-University Erlangen-Nürnberg.

The authors have access to the Biograph mMR PET/MR system installed at the Institute of Medical Physics, Friedrich-Alexander-University Erlangen-Nürnberg.

Reprints: Bharath K. Navalpakkam, MSc, Friedrich-Alexander-University Erlangen-Nürnberg, Henkestrasse 91, 91052, Erlangen, Germany. E-mail: Bharath.Navalpakkam@uk-erlangen.de.

ISSN: 0020-9996/13/4805–0323

fast acquisition and processing times necessary for clinical use.[16] Several groups have investigated the inclusion of the cortical bone as an attenuating class for brain PET-AC from atlas registration or dedicated MRI sequences such as ultrashort echo time (UTE) sequences, which are capable of visualizing the cortical bone and other structures with very short T2*.[13,17–19] Keereman et al[17] proposed a 3-class (air, soft tissue, cortical bone) segmentation approach from relaxation maps derived from UTE sequences and reported a 5% mean error across brain regions. Simulations from Catana et al[13] also confirmed the need for at least 3 classes—air, water, and cortical bone—because of differences in quantification for gray matter (GM), white matter, and cerebrospinal fluid regions. Berker et al[19] proposed a triple echo–based MR acquisition to identify cortical bone, water, and fat classes from 1 sequence.

An inherent drawback of all of the previously mentioned MR-based approaches is that they compare their segmentation results with a segmented patient CT. Although this approximation might hold true for attenuating classes such as air (Hounsfield units [HU] < −1000), GM, white matter, or fat (−300 < HU < 0), the wide range of CT voxel values for bone, 300 to 2000 HU, indicates the need for more than 1 class for its representation. Furthermore, as bone densities vary vastly across patients and across regions of the body, a discrete assignment of μ-values cannot adequately represent all bone voxels.[14]

Few attempts have been made to predict μ-values on a continuous scale from MR images. Hofmann et al[18,20] proposed pattern recognition methods by incorporating local neighborhood information from MR images in addition to an atlas registration step. They generate pseudo-CT images for each patient from T1-weighted spin-echo sequences. They have, however, not evaluated their approach on UTE sequences. Johansson et al[21] have derived substitute CTs from multiple MR acquisitions (2 UTE and 1 T2 weighted 3D spin echo based sequence) per patient using the Gaussian mixture model regression. Although their results look promising, lengthy acquisition times may limit its application to PET/MR. In the current study, a similar approach is followed, that is, to emulate a CT from a UTE and a 3D Dixon-VIBE sequence and, subsequently, to evaluate its efficacy on PET attenuation by comparing it with a patient CT as the criterion standard.

MATERIALS AND METHODS

Patient Examinations

Ten patients (4 females, 6 males; age, 50.6 ± 10.6 years; weight, 70.5 ± 9.1 kg) underwent a PET/CT scan on a Biograph 64 (Siemens AG, Healthcare Sector, Erlangen, Germany), followed by a PET/MR examination on a Biograph mMR (Siemens AG, Healthcare Sector, Erlangen, Germany) 137.2 ± 43.0 minutes after the PET/CT examination. All patients were administered with fluorodeoxyglucose (^{18}F-FDG) as a radiotracer (maximum, 246 MBq; minimum, 126 MBq). No additional tracer or radiation dose was administered for the PET/MRI examination. The patients were examined for a clinical question in the rest of the body and had no abnormalities in the brain. The clinical routine used for simultaneous PET/MR acquisitions for head scans includes a 3-plane localizer, a 3D Dixon-VIBE sequence, anatomical T1-turbo spin echo (TSE) and T2-TSE sequences, and an echo-planar-diffusion weighted sequence. In addition, for the purpose of this work, a UTE sequence was acquired. The PET acquisition time per bed position was set to 10 minutes. Because of the simultaneous acquisition of PET and MR data on the Biograph mMR system and the 10-minute PET acquisition time, the overall acquisition time was not prolonged by the additional UTE sequence. Altogether, the 3D Dixon-VIBE and the UTE sequences were used for the purpose of deriving MR-based attenuation maps. The UTE sequence was acquired with the following parameters: first echo time (TE1), 0.07 milliseconds; second echo time (TE2), 2.46 milliseconds; flip angle, 10 degrees; repetition time (TR), 11.94 milliseconds; field of view (FOV), 300 × 300 mm^2; slice thickness, 1.56 mm; acquisition matrix size, 192 × 192; and acquisition time, 84 seconds. The images were then reconstructed to a matrix size of 192 × 192 × 192 voxels with an isotropic voxel size of 1.56 × 1.56 × 1.56 mm^3. An optimized UTE sequence for studies of the head was provided by the vendor. No apparent differences due to geometrical distortion or scaling were noted between the 2 echoes. Second, a 2-point Dixon-VIBE sequence in 3D mode was acquired with the following parameters: voxel dimensions, 192 × 126 × 128; voxel size, 2.6 × 2.6 × 2.23 mm^3; TR, 3.6 milliseconds; TE, 1.23 milliseconds; flip angle, 10 degrees; and acquisition time, 19 seconds. For patient examinations, an approval from the Institutional Review and Ethical Board was obtained. All patients gave their informed and written consent.

Continuous Valued μ-Map Generation

Each of the 10 patients had 1 CT and 2 MR sequences (UTE and 3D Dixon-VIBE sequences), and the MR/CT pairs have identifiable air, cortical bone, water, and fat information available. Thus, a regression model is trained to learn this mapping between the 2 modalities considering the CT as the reference. The idea is to use the trained model to predict a pseudo-CT from the 2 MR sequences for a new patient, thereby making obsolete the need for a patient CT. The training was performed on 5 patients and the testing on the remaining 5 not used in the training step.

However, a prerequisite for model training is properly registered CT/MR data. After registration, an air mask is calculated. Furthermore, to better visualize the cortical bone, a difference map is calculated using the relation $S(x) = \ln I_1(x) - \ln I_2(x)$, where I_1 and I_2 represent UTE-TE1 and UTE-TE2 image intensities, respectively. Figure 1 shows the UTE-TE1, UTE-TE2, and the difference map. The air mask, together with CT, difference map, 3D Dixon-VIBE fat, and 3D Dixon-VIBE water images are used to train the regression model. A flow diagram is illustrated in Figure 2.

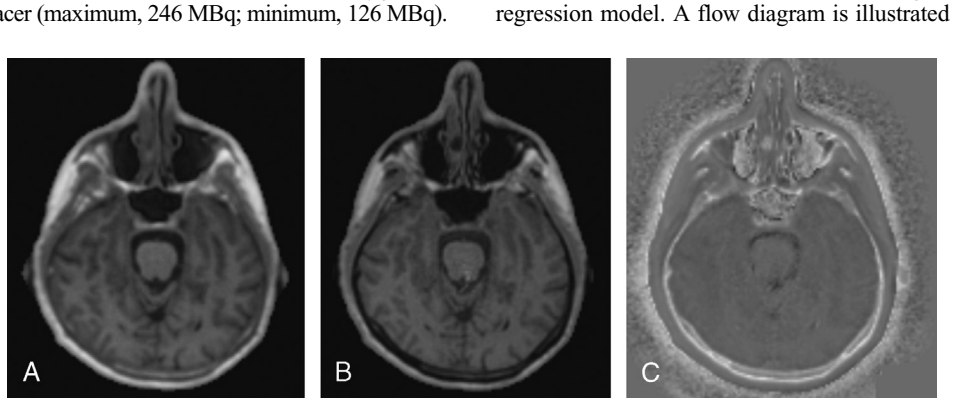

FIGURE 1. Distinguishing cortical bone from a UTE sequence: UTE-TE1 (A), UTE-TE2 (B), and difference map (C).

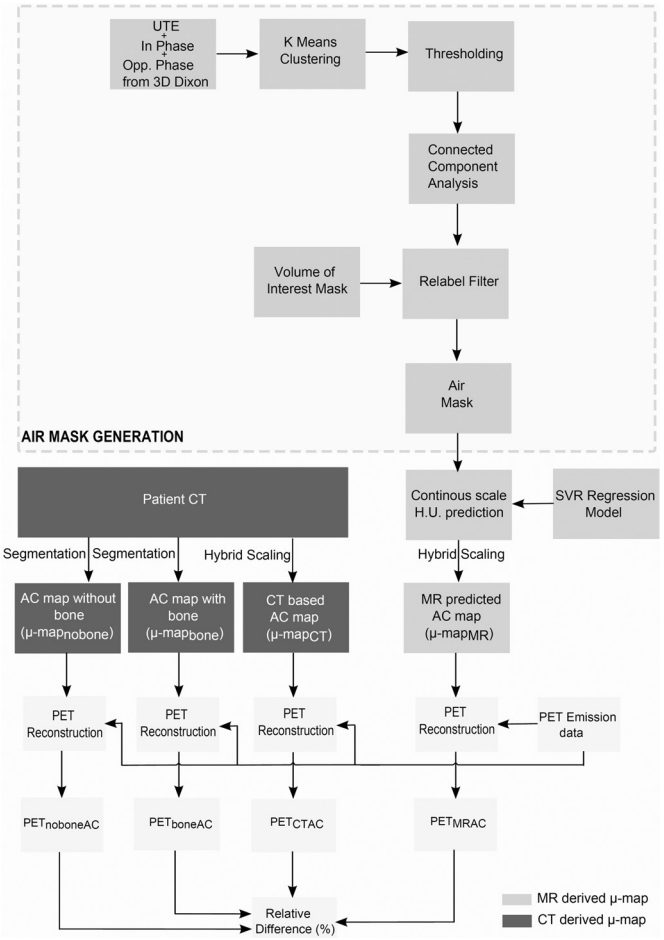

FIGURE 2. Positron emission tomographic attenuation correction pipeline. An air mask derivation allows for prediction of fat, water, and cortical bone class from MR sequences that result in $\mu\text{-map}_{MR}$. From the patient CT, 3 sets of μ-maps are derived: $\mu\text{-map}_{CT}$, $\mu\text{-map}_{nobone}$, and $\mu\text{-map}_{bone}$. The corresponding PET reconstructions are PET_{CTAC}, $PET_{noboneAC}$, PET_{boneAC}, and PET_{MRAC}. For each reconstruction, an RD image is calculated against PET_{CTAC} as the reference. The patient CT is only used for model training and evaluation and is not needed when predicting continuous valued μ-maps for a new patient.

Image Preprocessing

Because MR and CT data sets originate from the same patient and the focus was on the head region, a simple rigid transformation was sufficient to map the voxel correspondence. Furthermore, the patients in PET/CT are imaged in arms-up position; the patients in PET/MR, in arms-down position. In addition, the patient table and certain positioning aids not used in PET/MR are visible in the CT images. Therefore, as a preprocessing step, the patient bed and the positioning aids as well as the patients' arms were excluded from the CT volume to preserve the head alone to achieve better registration results. This cropped CT was then rigidly registered to the UTE-TE1 image using mutual information as the similarity measure. Subsequently, to eliminate the influence of possible patient motion between the acquisition of UTE-TE1 and the 3D Dixon-VIBE water images, these 2 images were also rigidly registered and the obtained transformation parameters were used in bringing the UTE-CT registered pair to the 3D Dixon-VIBE space. Finally, a visual assessment was done to check the registration result between the 2 modalities and no major discrepancies were noticed. All registrations were performed using the software elastix.[22] In a patient setup, however, the registration is not necessary because the CT images are only needed for an initial training. In the current study, only regions above the nose were considered for analysis.

Air Mask

The purpose behind a segmented air mask was to restrict the prediction of all other voxels to fat, water, or cortical bone because, in PET, high tracer uptakes are observed inside of this mask. This is necessary because misclassifying soft tissue for air in GM, for example, would underestimate considerably the PET activity for that voxel. A volume of interest (VOI) from UTE-TE1 was obtained through simple thresholding and morphological operations. Because high noise levels in the background of UTE-TE1 may result in an unreliable air segmentation, a voxelwise addition of the 3 volumes UTE-TE1, 3D Dixon-VIBE in-phase, and 3D Dixon-VIBE opposed-phase is performed. The composite image now has bone intensities from UTE-TE1, soft tissue information from the 3D Dixon-VIBE in-phase and opposed-phase images, but it has no signal from air in any of the sequences. The resulting image is then subjected to a scalar K-means classification with the sum of squared error metric. Altogether, 30 clusters were specified as an input to the algorithm together with initial cluster mean estimates starting from 0 to the maximum pixel value. An Otsu thresholding was then run to obtain a binary image.[23] To remove any stray segmentations that are not air, a connected component analysis was done on the binary image. A relabeling filter then sorted the identified components according to their weights in a descending manner. From this, the labels with the largest components greater than 1000 pixels were assigned to the air class. Finally, the air mask is obtained by multiplying the identified air class with the VOI mask (Fig. 3). To evaluate the generated air mask, predefined VOIs were placed and evaluated on commonly identified air regions on both CT and MR volumes as shown in Figure 4. All software processing was done using algorithms from Insight Toolkit.[24]

ε-Insensitive Support Vector Regression Training

Before the pseudo-CT estimation, a model generation step is necessary to learn the mapping between the associated classes from the extracted MR feature vectors to their corresponding CT HU. A pattern recognition approach ε-SVR is used for this purpose.[25,26] Given a feature vector $\{\vec{x}_1, \vec{x}_2, \vec{x}_3 \ldots \vec{x}_l\}$, where $\vec{x}_i \in R^l$ and their corresponding target responses $\{y_1, y_2, y_3 \ldots y_l\}$, $y_i \in R^1$, ε-SVR attempts to find a suitable mapping $f(\vec{x})$ as close as possible to y_i with most ε errors. This can be visualized as having an ε-insensitive tube around the target values y_i. The decision function $f(\vec{x})$ is obtained by solving the following convex optimization problem:

$$\min_{\vec{w},\xi,\xi^*} P = \frac{1}{2}\vec{w}^T\vec{w} + C\sum_{i=1}^{l}(\xi + \xi^*) \quad (1)$$

subject to

$$y_i - \langle\vec{w}, \phi(\vec{x})\rangle + b \leq \varepsilon + \xi \quad (2)$$

$$\langle\vec{w}, \phi(\vec{x})\rangle + b - y_i \leq \varepsilon + \xi^* \quad (3)$$

$$\xi_i, \xi^* \geq 0 \quad (4)$$

Here, $i = 1,2 \ldots l$, where l is the number of training instances, ξ,ξ^* represent slack variables that are 0 if the error is within ε range and nonzero otherwise, $\langle,\rangle$, the dot product operator, $\vec{w}$, the normal vector to the hyperplane, and b is the bias. The constant C is a trade-off factor that controls the number of misclassifications beyond ε and

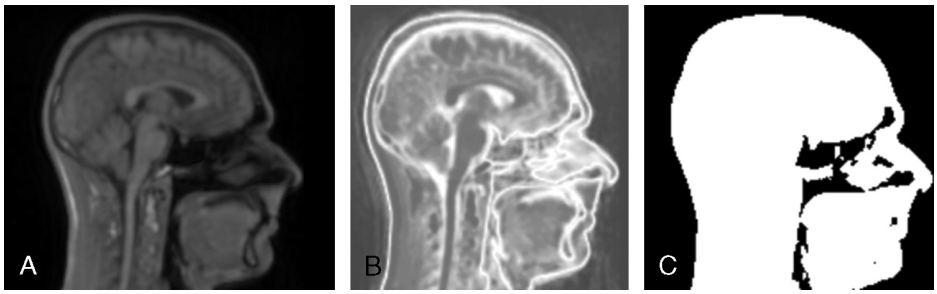

FIGURE 3. Air mask steps. A, Voxelwise addition from UTE-TE1 and in-phase and opposed phase images. B, Result of K-means classification. C, Air mask obtained from connected component analysis. The regression model prediction can now be restricted to fat, water, and cortical bone inside the air mask.

the flatness of the decision boundary. $<\vec{w}, \phi(\vec{x})>$ represents the dot product in the feature space p, where $\phi : \vec{x} \rightarrow p$. The input vectors $\vec{x}$ are projected to a higher dimensional feature space p, where a decision boundary is determined through a nonlinear mapping function $\phi(\vec{x})$. A kernel function $K(\vec{x_i}, \vec{x_j})$ can be described in terms of the mapping function through a dot product in the feature space p.

$$K(\vec{x_i}, \vec{x_j}) = <\phi(\vec{x_i}), \phi(\vec{x_j})> \quad (5)$$

With this formulation (equation 5), the mapping of input vectors $\vec{x}$ to feature space p can be done implicitly via the kernel function. For more details on ε-SVR, please refer to the studies of Vapnik[25] and Smola and Schölkopf.[26] For this study, a radial basis kernel $K(\vec{x_i}, \vec{x_j})$ was chosen as the kernel function.

$$K(\vec{x_i}, \vec{x_j}) = e^{-\gamma \|\vec{x_i} - \vec{x_j}\|^2} \quad (6)$$

The decision function for a new feature vector $\vec{x}$ can be formulated as follows:

$$f(\vec{x_i}, \alpha_i, \alpha_i^*) = \sum_{i=0}^{l} (\alpha_i - \alpha_i^*) K(\vec{x_i}, \vec{x_j}) + b \quad (7)$$

where γ is the width of the RBF kernel and α_i, α_i^* are Lagrange multipliers and $0 \leq \alpha_i, \alpha_i^* \leq C$. The extracted features include mean, median, variance, and maximum and minimum values across a $3 \times 3 \times 3$ local neighborhood from 3D Dixon-VIBE fat, 3D Dixon-VIBE water, and difference map volumes. A soft margin is used with slackness constraints ξ, ξ^* to allow errors beyond the ε-insensitive tube while, at the same time, penalizing the cost function. Altogether, 5 quadruplets of images were used for training and validation. A random subset was extracted from the training instances of the 5 patients, and a subsequent grid search was performed to determine optimal parameters of (C, γ, ε) through a 5-fold cross validation method to avoid overfitting. All pattern recognition processing was done using the library for support vector machines.[27]

Generation of Continuous Valued μ-Maps for Patients Not Included in the Training Process

For a new patient, an air mask is generated as described previously and features across $3 \times 3 \times 3$ are extracted from MR images: difference map, 3D Dixon-VIBE fat, and 3D Dixon-VIBE water images. The trained ε-SVR model is then used to predict HU on a continuous scale for fat, water, and cortical bone classes inside of the air mask.

Evaluation

Attenuation Maps

Four μ-maps were generated: (1) patient CT ($\mu\text{-map}_{CT}$), (2) MR-predicted CT ($\mu\text{-map}_{MR}$), (3) 4-class segmented CT with bone ($\mu\text{-map}_{bone}$), and (4) 3-class 3D Dixon-VIBE–like CT without bone ($\mu\text{-map}_{nobone}$). Figure 5 shows the different μ-maps used for comparison. The first 2 ($\mu\text{-map}_{CT}$ and $\mu\text{-map}_{MR}$) were converted to PET energy (511 keV) by hybrid scaling[4] and the third ($\mu\text{-map}_{bone}$) was thresholded into air (HU < -300), fat ($-300 \leq$ HU < 0), water ($0 \leq$ HU< 300), and bone (HU ≥ 300), and LACs of 0 cm^{-1}, 0.1000 cm^{-1}, 0.0854 cm^{-1}, and 0.1510 cm^{-1} were assigned, respectively. $\mu\text{-Map}_{nobone}$ was constructed by assigning 0 cm^{-1}, 0.0854 cm^{-1}, and 0.1000 cm^{-1} from thresholding CT into air (HU < -300), fat ($-300 \leq$ HU < 0), and water (HU ≥ 0), respectively. Refer to Figure 2 for an overall PET processing pipeline.

For studies of the head, the total acquisition time was 103 seconds: 19 seconds for 3D Dixon-VIBE and 84 seconds for the UTE acquisition.

The generation of $\mu\text{-map}_{MR}$ on an Intel Xeon processor with 8 cores took approximately 3 minutes.

Reconstruction Parameters and Evaluation of Quantification

Attenuation-corrected PET data reconstructed from the previously mentioned μ-maps ($\mu\text{-map}_{CT}$, $\mu\text{-map}_{MR}$, $\mu\text{-map}_{bone}$, $\mu\text{-map}_{nobone}$)

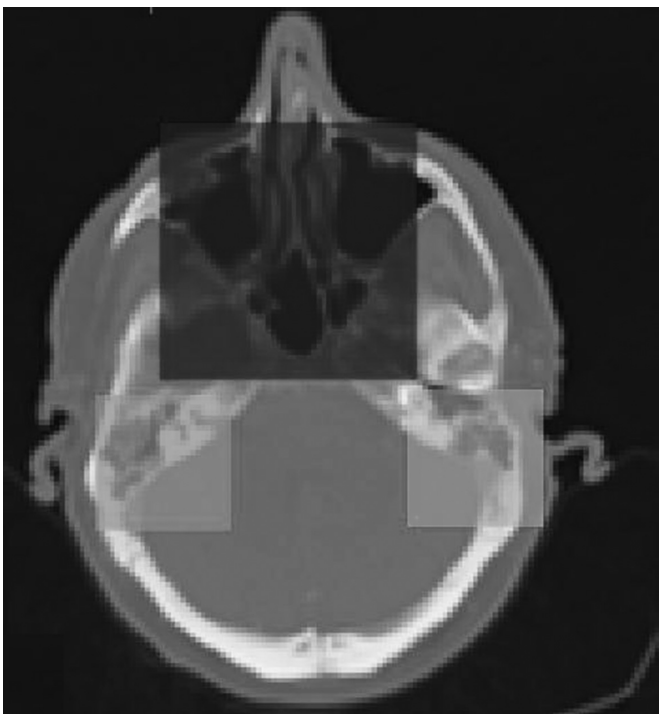

FIGURE 4. Sample placements of VOIs around air regions.

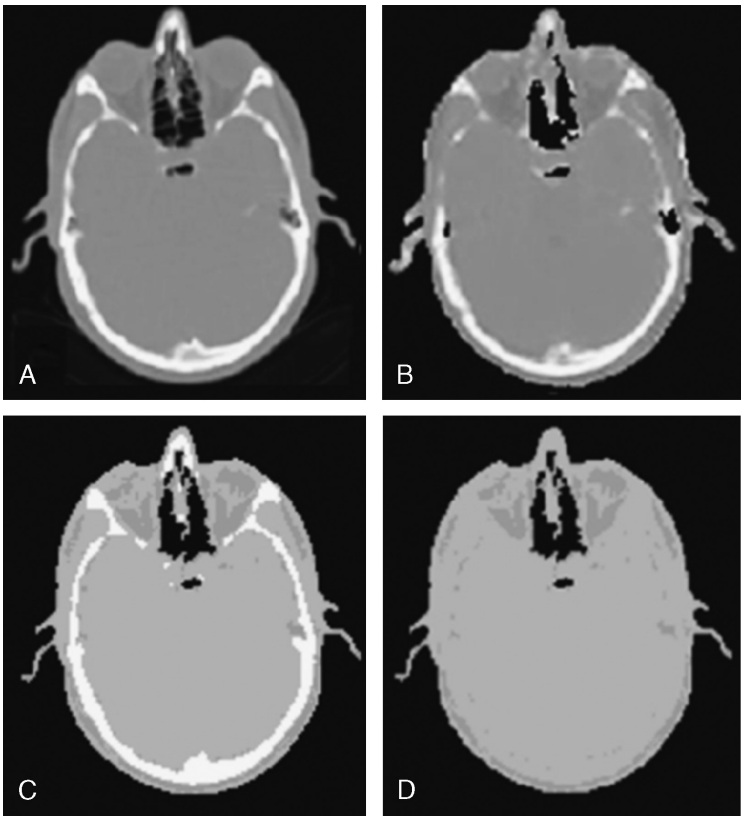

FIGURE 5. Different attenuation maps used for comparison. Transaxial slices of patient P3: patient CT, μ-map$_{CT}$ (A); MR-predicted CT, μ-map$_{MR}$ (B); 4-class segmented CT with bone, μ-map$_{bone}$ (C), 3-class 3D Dixon-VIBE–like CT without bone, μ-map$_{nobone}$ (D).

will be referred to as PET_{CTAC}, PET_{MRAC}, PET_{boneAC}, and $PET_{noboneAC}$, respectively. All reconstructions were performed on the Biograph mMR console with standard settings: ordered subset expectation maximization with 3 iterations, 21 subsets, post smoothed with a 4-mm full-width-at-half-maximum Gaussian low pass filter with enabled scatter correction. The complete brain was segmented from UTE-TE2 and 3D Dixon-VIBE opposed-phase images for the purpose of analyzing global PET quantification differences between the reconstructed results. Furthermore, to analyze local PET uptake differences, 13 landmarks close to the cortical bone were segmented on the basis of GM regions. All segmentations were performed using the software IBASPM.[28] A relative difference (RD) image is calculated using the relation $\alpha(x) = 100^* \frac{\left(PET_i(x) - PET_{CTAC}(x)\right)}{PET_{CTAC}(x)}$, where i represents the different μ-maps, that is, CT, MR, no bone, and bone. In addition, a linear regression analysis with the following relation $y=mx+c$ was performed, where x and y denote the activities from PET_{CTAC} and PET_{MRAC} PET_{boneAC}, and $PET_{noboneAC}$.

RESULTS

Air Mask Evaluation

The overall air classification rate per patient is enlisted in Table 1. The mean correctly classified air rate was 76.23% across all patients for the drawn VOIs. Most deviations were observed at the air-soft tissue and bone-soft tissue interfaces where MR susceptibility artifacts limit a precise segmentation.

Positron Emission Tomographic Comparisons

Exemplary slices of the RD volumes for PET reconstructions are shown in Figure 6. From a qualitative standpoint, both PET_{MRAC} and PET_{CTAC} are in good agreement. No misleading or artifactual uptake spots were introduced by the algorithm. Quantitatively, a constant underestimation is observed for $PET_{noboneAC}$ for all patients (red coloration) because of cortical bone omission. For all patients, PET_{boneAC} resulted in small underestimations within 5% (light-red coloration) because of the lower LAC for water 0.1000 cm^{-1} in μ-map$_{bone}$ in contrast to μ-map$_{CT}$.

The global error difference on PET due to different attenuation maps is seen in Table 2. Table 3 shows the results of PET quantification for regions close to the cortical bone for all reconstructions. The exclusion of the cortical bone resulted in noticeable underestimations for $PET_{noboneAC}$ that produced a global error of 10.15% ± 3.31% and 11.03% ± 2.26% error close to the cortical

TABLE 1. Patient-Specific Air Classification Rate (%)

Patient	Correct Air Classification (%)
P1	81.73
P2	84.57
P3	73.28
P4	63.63
P5	77.96
Mean	76.23

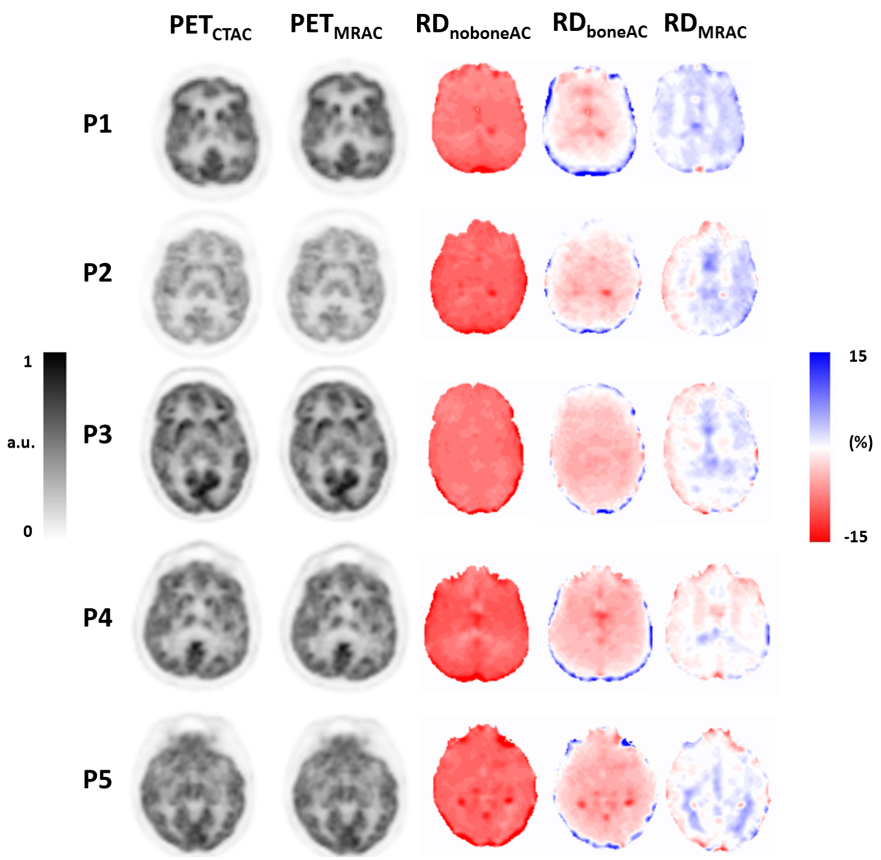

FIGURE 6. Positron emission tomographic volumes reconstructed from different attenuation maps. Visually, PET_{MRAC} compares well with PET_{CTAC}. PET_{MRAC} compares with PET_{CTAC} with an error of 2.40% ± 3.69% for the entire brain and 2.16% ± 1.77% for the regions close to the cortical bone. Red and blue colorations indicate underestimation and overestimation errors, respectively.

bone. On the other hand, the overestimations due to constant LAC for the cortical bone in PET_{boneAC} translated to a local overestimation error of 4.22% ± 3.91% close to the cortical bone but had no severe global impact (3.96% ± 3.71%) because the nature of these local errors decreased with increasing distance from the soft tissue and cortical bone interface. The PET_{MRAC} was able to estimate PET activities with an error of 2.40% ± 3.69% for the brain regions and 2.16 ± 1.77% for the regions close to the cortical bone. Large mean and standard deviation values for PET_{boneAC} for the segmented landmarks in Table 3 demonstrate the variability in the LAC assignment close to the skull. Errors reported are averaged across all patients and are in absolute units.

Considering the proximity of GM to the skull, the effect of segmented μ-maps on PET quantification and the benefit of using continuous density LAC assignments can be seen in Figure 7. The proposed method minimizes these estimation errors at the skull periphery in contrast to more than 10% errors for $PET_{noboneAC}$

TABLE 2. Positron Emission Tomographic Quantification Differences on the Complete Brain for All 5 Patients

Patients	RD_{MRAC}	$RD_{noboneAC}$	RD_{boneAC}
P1	2.84 (4.18)	10.25 (3.62)	4.22 (3.62)
P2	2.18 (3.29)	10.48 (4.02)	4.43 (4.66)
P3	2.42 (3.21)	10.75 (2.84)	3.57 (4.00)
P4	2.26 (4.29)	9.22 (3.08)	3.56 (2.82)
P5	2.28 (3.48)	10.05 (2.98)	4.03 (3.44)
Mean	2.40 (3.69)	10.15 (3.31)	3.96 (3.71)

All values are expressed as mean (SD) and in percentage (%).

TABLE 3. Summary of PET Activity Differences on Segmented Regions Across All Patients and for All PET Reconstructions

Landmarks	RD_{MRAC}	$RD_{noboneAC}$	RD_{boneAC}
Angular gyrus LR	2.35 (1.97)	10.88 (2.28)	4.79 (4.65)
Cuneus LR	2.49 (1.17)	11.17 (2.86)	4.07 (4.21)
Inferior frontal gyrus LR	2.25 (1.94)	9.97 (2.14)	3.80 (4.35)
Middle frontal gyrus LR	1.84 (1.50)	10.28 (1.60)	3.88 (3.45)
Middle occipital gyrus LR	2.24 (1.73)	12.13 (2.70)	4.72 (3.65)
Occipital lobe LR	3.45 (2.64)	15.10 (3.20)	6.07 (4.65)
Postcentral gyrus LR	1.97 (1.61)	10.59 (2.00)	4.43 (4.35)
Precentral gyrus LR	2.19 (1.70)	10.17 (2.12)	3.85 (4.55)
Superior frontal gyrus LR	1.55 (1.19)	9.78 (1.55)	3.66 (2.19)
Superior occipital gyrus LR	1.83 (1.43)	12.58 (3.04)	5.38 (5.37)
Superior parietal lobule LR	1.32 (1.16)	10.81 (2.42)	3.72 (3.86)
Superior temporal gyrus LR	2.30 (1.72)	9.84 (1.57)	2.87 (1.79)
Supramarginal gyrus LR	2.63 (2.67)	10.09 (1.80)	3.61 (3.71)
Mean	2.16 (1.77)	11.03 (2.26)	4.22 (3.91)

In general, PET_{MRAC} estimates accurately PET_{CTAC} than any other method does.
All values are expressed as mean (SD) and in percentage (%).
LR indicates left right.

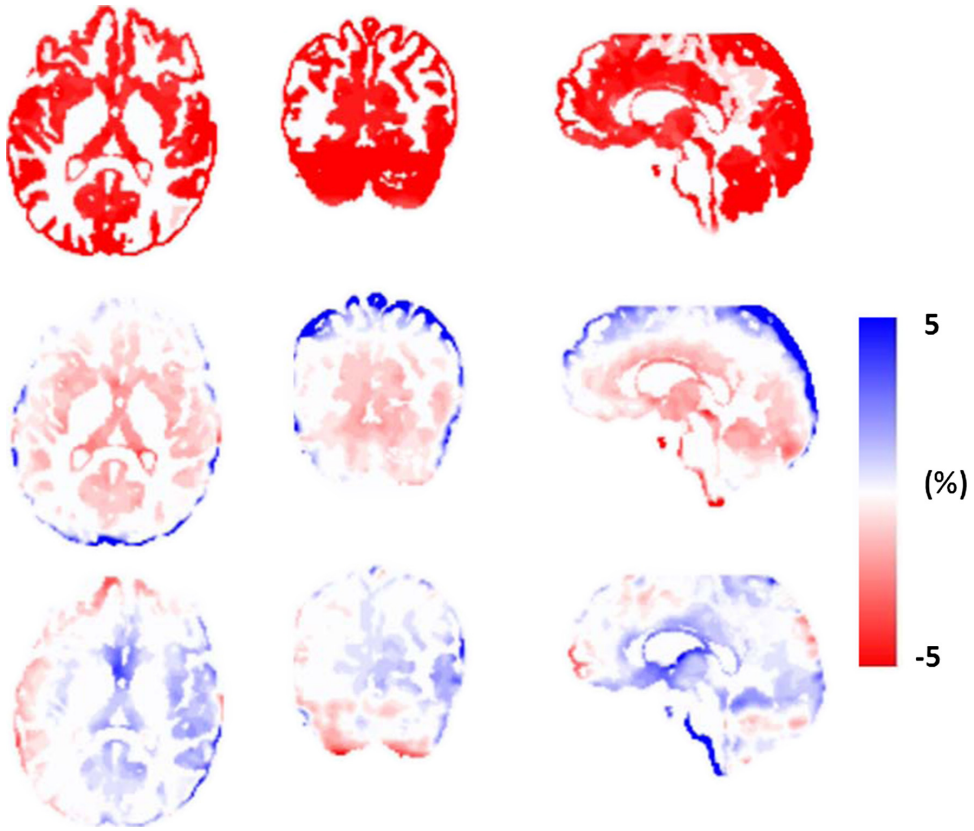

FIGURE 7. Effect of segmentation-based attenuation maps on PET-AC for patient P2. Illustration shows the RD maps on GM regions (compared with the criterion standard): $PET_{noboneAC}$ (top row), PET_{boneAC} (middle row), and PET_{MRAC} (bottom row). A consistent error greater than 11% (underestimation) at the periphery of the skull in $PET_{noboneAC}$ and greater than 4% (overestimation) in PET_{boneAC} has been improved in PET_{MRAC} because of continuous bone density prediction. Red and blue colorations indicate underestimation and overestimation errors, respectively.

and 4% errors for PET_{boneAC}. The overestimation errors can be thought of as bone intraclass misclassifications where the assigned LAC is offset by a large degree compared with the actual value in the CT.

A scatterplot of PET activities with calculated regression lines for the segmented landmarks is shown in Figure 8. The PET_{MRAC} has a near-unity slope (1.012) compared with $PET_{noboneAC}$ (0.918) or PET_{boneAC} (0.961), indicating that the proposed method has the potential to estimate PET activities accurately with respect to the criterion standard. Table 4 shows the coefficient of determination (R^2) and regression coefficients.

Also, for a patient not included in this study, because of a different injected tracer, the proposed approach was able to predict calcifications in the brain regions. Figure 9 shows the comparison between the MR-predicted CT and the patient CT.

Figure 10 shows PET_{MRAC} overlayed on an anatomical T2-TSE sequence. The conjunction of high soft tissue contrast from the MR is seen with functional information from PET.

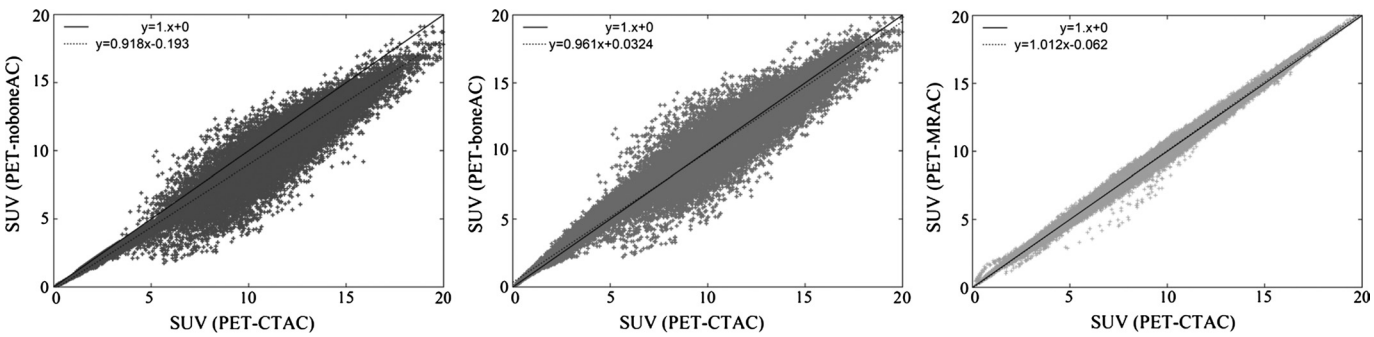

FIGURE 8. Scatterplots from $PET_{noboneAC}$, PET_{boneAC}, and PET_{MRAC} with respect to PET_{CTAC} as reference for all patients. Comparatively, PET_{MRAC} has a closer-to-identity slope than any other method does.

TABLE 4. Results of Linear Regression Analysis on PET Activities From the Investigated Attenuation Maps

Coefficients	PET_{MRAC}	$PET_{noboneAC}$	PET_{boneAC}
m	1.012 (0.000)	0.918 (0.000)	0.961 (0.000)
c	−0.062 (0.002)	−0.193 (0.003)	0.0324 (0.004)
R^2	0.994 (0.218)	0.972 (0.425)	0.961 (0.527)

Pelvis Attenuation Maps

An accurate MR to CT mapping is a prerequisite for optimal model training. This is not straightforward to achieve even for an intrapatient whole-body scenario because of inherent physiological motion and different patient configurations (arms up in PET/CT, arms down in PET/MR). To circumvent this problem, the model generated for studies of the head is reused on other stations, assuming that the classifier generalization holds good.

First, a manual thresholding procedure was used for creating an initial mask, followed by a morphological closing operation to generate an air mask. The voxels inside the mask were assigned continuous HU values calculated by the ε-SVR. The volunteers were scanned using the same acquisition protocols as described for studies of the head with no acquired emission data. The estimated pseudo-CT is shown in Figure 11. The overall processing time for deriving the pelvis attenuation map was approximately 7 minutes. However, a drawback with the UTE sequence used in this study is the limited FOV, which is 300 mm × 300 mm. In voxels beyond these regions, where there is an absence of UTE signal, the model predicts water/fat intensities from the 3D Dixon-VIBE sequence. This setting allows the assignment of cortical bone LACs when possible or at least water/fat, otherwise. This is important especially for patients with obesity wherein a complete pelvic bone coverage due to UTE may be not guaranteed.

DISCUSSION

A method to generate pseudo-CTs via ε-SVR is presented and is evaluated toward PET quantification. The approach was validated for 5 patients who had MR/PET/CT triplets and evaluated for the remaining 5 patients not included in the model-generation process. The patient CT was a prerequisite for training the classifier and can be dropped once a model has been generated and when estimating a pseudo-CT for a new patient.

The evaluation was done for the proposed method against different attenuation maps comprising of the scaled CT, the segmented CT (with cortical bone), and the segmented CT (without cortical bone). Attenuation-corrected PET images from the proposed method compare well both qualitatively and quantitatively to the other approaches (Fig. 6). Figure 8 suggests that the proposed continuous valued pseudo-CT method is feasible for studies of the head and is in better agreement to the criterion standard than the currently used 3-class approach is.

Because the head is a more compact region and the cortical bone is a high-attenuation medium, it requires a careful LAC assignment for accurate PET quantification. In this context, UTE sequences have already been used for the purpose of attenuation correction. Catana et al[13] and Keereman et al[17] proposed segmentation-based approaches based on UTE for PET-AC and compared their results with a segmented CT. Although segmented CT has no significant global influence on PET quantification, it yields regionally increased errors close to the skull periphery (Fig. 7). The proposed method minimizes this bias. However, a classifier training across a larger patient collective would be useful for obtaining accurate LAC estimations.

Similarly, for both the brain and close to the cortical bone regions, $PET_{noboneAC}$ underestimated activities by at least 10% consistently across all patients. This decrease is also in agreement with errors 10% to 15% underestimation reported by Schramm et al,[11] Samarin et al,[12] and Catana et al,[13] reiterating the inclusion of a cortical bone class when deriving μ-maps. Although cortical bone exclusion can be generally accepted for whole-body studies, its application has limitations toward neurological studies.[8,9]

The following observations were made when deriving the attenuation maps. During mask generation, the air mask omitted fine structures at the ethmoid sinus and parts of the middle ear cavities (mastoid air cells and tympanic cavities). Although no global impact was observed, the effect of this misclassification led to error variations up to 30% in the adjacent structures. As an improvement, multiple UTE sequences with different acquisition parameters (eg, flip angle, TE) can also be used.[21] This could give more T2* information per voxel that could result in better model generalization. However, with this approach, it is not clear as to which HU would the classifier predict for very fine tissues, given the susceptibility artifacts. Also, patient acquisition times and motion are its biggest limitations.

Not included in this study were also regions below the nose where uncertainties are vast, for example, differences in tongue, swallowing, and uvula positions, and this may introduce potential

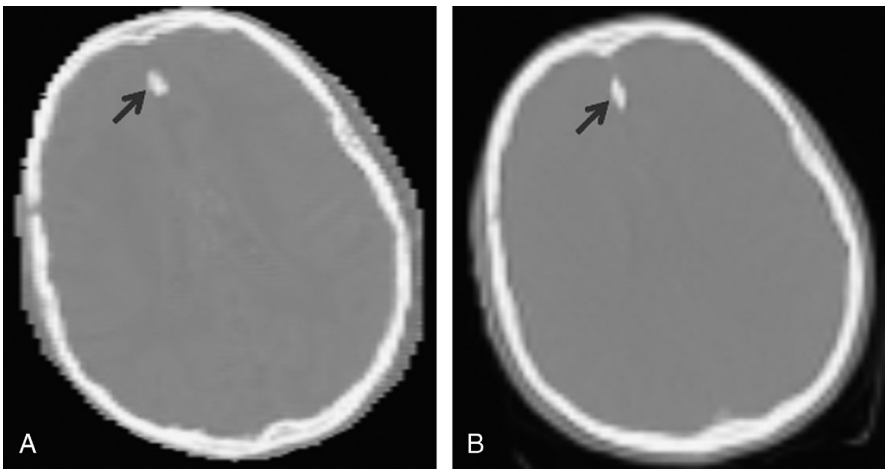

FIGURE 9. Magnetic resonance–predicted CT (A) is able to identify calcifications (arrows) in comparison with the patient CT (B).

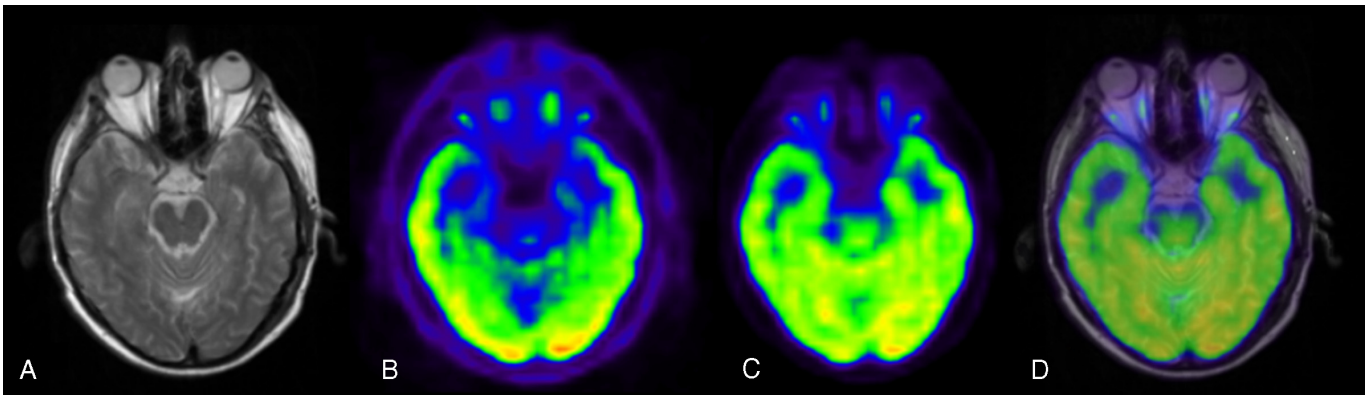

FIGURE 10. Anatomical T2 turbo spin echo sequence (A), non-attenuation corrected PET (B), PET_{MRAC} (C), and fused PET/MR (C overlayed on A) (D).

bias for PET comparisons. Also ignored were the dental regions and implants where a CT is unlikely to serve as a reference because of metal streak artifacts.

For older patients, underestimation of hot spots were observed because of the inherent calcifications in the brain for PET_{boneAC} reconstruction. This resulted in RD of 5% to 10% because of its local assignment as a soft tissue (0.1000 cm^{-1} in μ-map_{bone}). The proposed method underestimated PET activities with the same error range as the regression model estimated soft-tissue HU for these regions. This was because, in patient P4, the UTE sequence was not sensitive enough to highlight these intensities. In the patient CT, this region corresponded to less than 200 HU. However, in another patient who was not included in this study, the calcifications were predicted by the model and their corresponding intensities were greater than 500 HU in the patient CT. This can be seen in Figure 9.

Reconstructed PET_{MRAC} may also include slight misregistrations between the pseudo-CT and the patient CT. This is inherently overcome for segmentation-based μ-maps because the reference CT is used for this purpose. Also, the protruding ear regions and, subsequently, the outer sheath of the skin are oversegmented for mask consideration by the morphological closing operator. These contribute to errors as a voxel-to-voxel difference is performed, and they are treated as misclassifications.

Besides ^{18}F-FDG, generated pseudo-CTs can motivate investigation into other hybrid imaging systems such as single-photon emission computed tomography (SPECT)/CT where patient CT is used for attenuation and scatter correction together with a possibility of imaging multiple radiopharmaceuticals such as technetium-99 (^{99}Tc) or iodine-131 (^{131}I). Although initial results in SPECT/MR technical integration have been reported, certainly, an MRAC seems promising.[29]

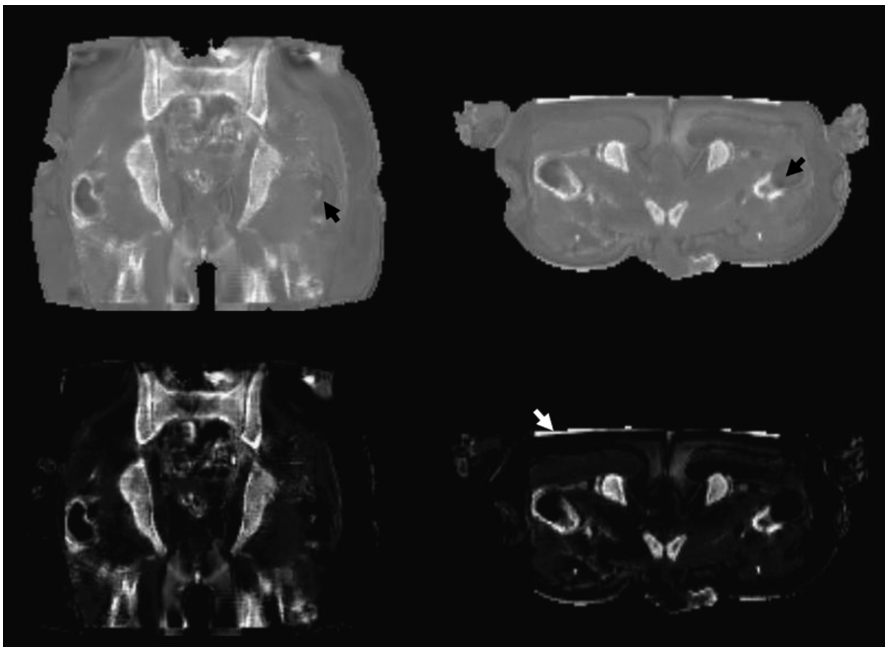

FIGURE 11. Top row, Coronal and transaxials views of MR-predicted CT using model generated for brain studies. Bottom row, Window/level adjusted views for the same volunteer. The model predicts cortical bone where both UTE and 3D Dixon-VIBE information is available or simply water/fat in the absence of UTE intensities (black arrows). Some voxels were misclassified as bone because of oversegmentation by the masking procedure (white arrow). The UTE sequence had a limited FOV (300 mm $\times$ 300 mm).

Lastly, our model can be reused on other regions of the body. Figure 11 shows initial results where the pelvic bone discrimination is seen and could be of potential benefit for studies targeting prostate cancer. As a further improvement, more accurate pseudo-CTs could be generated via separate model training for each coil/body region using UTE with 3D Dixon-VIBE or other sequences. However, this effect on PET has not been investigated yet and is a part of ongoing research.

CONCLUSIONS

In this study, the generation of continuous valued attenuation maps from MR sequences is demonstrated and its effect on PET quantification is evaluated in comparison with segmentation-based μ-maps. A less-than-2-minute acquisition time makes the proposed approach promising for a clinical application for studies of the head. However, further experiments are required to validate and evaluate this technique for attenuation correction in other regions of the body.

ACKNOWLEDGMENT

The authors gratefully acknowledge the funding from the International Max Planck Research School for Physics of Light (IMPRS-PL).

REFERENCES

1. Pichler BJ, Kolb A, Naegele T, et al. PET/MRI: paving the way for the next generation of clinical multimodality imaging applications. *J Nucl Med*. 2010; 51:333–336.
2. Zaidi H, Del Guerra A. An outlook on future design of hybrid PET/MRI systems. *Med Phys*. 2011;38:5667–5689.
3. Drzezga A, Souvatzoglou M, Eiber M, et al. First clinical experience with integrated whole-body PET/MR: comparison to PET/CT in patients with oncologic diagnoses. *J Nucl Med*. 2012;53:845–855.
4. Wiesmüller M, Quick HH, Navalpakkam B, et al. Comparison of lesion detection and quantitation of tracer uptake between PET from a simultaneously acquiring whole-body PET/MR hybrid scanner and PET from PET/CT. *Eur J Nucl Med Mol Imaging*. 2013;40:12–21.
5. Boss A, Kolb A, Hofmann M, et al. Diffusion tensor imaging in a human PET/MR hybrid system. *Invest Radiol*. 2010;45:270–274.
6. Kinahan PE, Townsend DW, Beyer T, et al. Attenuation correction for a combined 3D PET/CT scanner. *Med Phys*. 1998;25:2046–2053.
7. Kinahan PE, Bruce HH, Beyer T. X-ray–based attenuation correction for positron emission tomography/computed tomography scanners. *Semin Nucl Med*. 2003;33:166–179.
8. Martinez-Möller A, Souvatzoglou M, Delso G, et al. Tissue classification as a potential approach for attenuation correction in whole-body PET/MRI: evaluation with PET/CT data. *J Nucl Med*. 2009;50:520–526.
9. Schulz V, Espallarado IT, Renisch S, et al. Automatic, three-segment, MR-based attenuation correction for whole-body PET/MR data. *Eur J Nucl Med Mol Imaging*. 2011;38:138–152.
10. Keller SH, Holm S, Hansen AE, et al. Image artifacts from MR-based attenuation correction in clinical, whole-body PET/MRI. *MAGMA*. 2013; 26:173–181.
11. Schramm G, Langner J, Hofheinz F, et al. Quantitative accuracy of attenuation correction in the Philips Ingenuity TF whole-body PET/MR system: a direct comparison with transmission-based attenuation correction. *MAGMA*. 2013; 26:115–126.
12. Samarin M, Burger C, Wollenweber SD, et al. PET/MR imaging of bone lesions—implications for PET quantification from imperfect attenuation correction. *Eur J Nucl Med Mol Imaging*. 2012;39:1154–1160.
13. Catana C, Van der Kouwe A, Benner T, et al. Toward implementing an MRI-based PET attenuation-correction method for neurologic studies on the MR-PET brain prototype. *J Nucl Med*. 2010;51:1431–1438.
14. Keereman V, Holen RV, Mollet P, et al. The effect of errors in segmented attenuation maps on PET quantification. *Med Phys*. 2011;38:6010–6019.
15. Kim JH, Lee JS, Song IC, et al. Comparison of segmentation-based attenuation correction methods for PET/MRI: evaluation of bone and liver standardized uptake value with oncologic PET/CT data. *J Nucl Med*. 2012;53:1878–1882.
16. Bezrukov I, Mantlik F, Schmidt H, et al. MR-based PET attenuation correction for PET/MR imaging. *Semin Nucl Med*. 2012;43:45–49.
17. Keereman V, Fierens Y, Broux T, et al. MRI-based attenuation correction for PET/MRI using ultrashort echo time sequences. *J Nucl Med*. 2010;51: 812–818.
18. Hofmann M, Steinke F, Scheel V, et al. MRI-based attenuation correction for PET/MRI: a novel approach combining pattern recognition and atlas registration. *J Nucl Med*. 2008;49:1875–1883.
19. Berker Y, Franke J, Salomon J, et al. MRI-based attenuation correction for hybrid PET/MRI systems: a 4-class tissue segmentation technique using a combined ultrashort-echo-time/Dixon MRI sequence. *J Nucl Med*. 2012;53: 796–804.
20. Hofmann M, Bezrukov I, Mantlik F, et al. MRI-based attenuation correction for whole-body PET/MRI: quantitative evaluation of segmentation- and atlas-based methods. *J Nucl Med*. 2011;52:1392–1399.
21. Johansson A, Karlsson M, Nyholm T. CT substitute derived from MRI sequences with ultrashort echo time. *Med Phys*. 2011;38:2708–2714.
22. Murphy K, Viergever MA, Pluim JPW, et al. Elastix: a toolbox for intensity based medical image registration. *IEEE Trans Med Imaging*. 2010;29:196–205.
23. Otsu N. A threshold selection method from gray level histograms. *IEEE Trans Syst Man Cybern*. 1979;9:62–66.
24. Insight Segmentation and Registration Toolkit. Available at: http://www.itk.org. Accessed Feb 15, 2012.
25. Vapnik V. *The Nature of Statistical Learning Theory*. New York, NY: Springer; 1995.
26. Smola A, Schölkopf B. A tutorial on support vector regression. *NeuroCOLT2 Techn Rep Ser*. 2004;30:199–222.
27. Chang CC, Lin CJ. LIBSVM: a library for support vector machines. *ACM Trans Intell Syst Technol*. 2011;2:1–27.
28. Alemán-Gómez Y, Melie-García L, Valdés-Hernandez P. IBASPM: toolbox for automatic parcellation of brain structures. In: 12th Annual Meeting of the Organization for Human Brain Mapping; June 11-15, 2006; Florence, Italy. Available on CD-Rom in NeuroImage, vol. 27, no. 1.
29. Hamamura MJ, Ha S, Roeck WW, et al. Development of an MR compatible SPECT system (MRSPECT) for simultaneous data acquisition. *Phys Med Biol*. 2010;55:1563–1575.

Noninvasive Nodal Staging in Patients With Breast Cancer Using Gadofosveset-Enhanced Magnetic Resonance Imaging: A Feasibility Study: Erratum

In the article that appeared on page 134 of the March issue of *Investigative Radiology*, in the reprint section, the author's first name is omitted. The author's name should have been "Regina G.H. Beets-Tan". We regret the error.

REFERENCE

Schipper R-J, Smidt ML, van Roozendaal LM, et al. Noninvasive nodal staging in patients with breast cancer using gadofosveset-enhanced magnetic resonance imaging: a feasibility study. *Invest Radiol*. 2013;48:134–139.